Progress In Electromagnetics Research, Vol. 140, 613–631, 2013

A NEW EFIE METHOD BASED ON COULOMB GAUGE FOR THE LOW-FREQUENCY ELECTROMAGNETIC ANALYSIS

Xiaoyan Y. Z. Xiong*, Li Jun Jiang, Wei E. I. Sha, and Yat Hei Lo

Department of Electrical and Electronic Engineering, the University of Hong Kong, Pokfulam Road, Hong Kong, China

Abstract—To solve the low-frequency breakdown inherent from the electric field integral equation (EFIE), an alternative new form of the EFIE is proposed by using the Coulomb-gauge Green's function of quasi-static approximation. Different from the commonly adopted Lorentz-gauge EFIE, the Coulomb-gauge EFIE separates the solenoidal and irrotational surface currents explicitly, which captures inductive and capacitive responses through electrodynamic and electrostatic Green's functions, respectively. By applying existing techniques such as the loop-tree decomposition, frequency normalization, and basis rearrangement, the Coulomb-gauge EFIE also can remedy the low-frequency breakdown problem. Through comparative studies between the Lorentz-gauge and Coulomb-gauge EFIE approaches from mathematical, physical and numerical aspects, the Coulomb-gauge EFIE approach shows the capability of solving low-frequency problems and achieves almost the same accuracy and computational costs compared to the Lorentz-gauge counterpart.

1. INTRODUCTION

The electric field integral equation (EFIE) method is one of commonly-adopted methods for modern simulations of scattering, radiation, and circuit problems [1, 2]. The popularity of the EFIE stems from the efficient surface triangulation, excellent numerical precision, and powerful capabilities to handle open and complex geometries. However, when the frequency tends to zero, the method-of-moment (MoM) solution of the EFIE using the Rao-Wilton-Glisson (RWG) basis

Received 3 April 2013, Accepted 18 June 2013, Scheduled 26 June 2013

* Corresponding author: Xiaoyan Y. Z. Xiong (xyxiong@eee.hku.hk).

functions [3] suffers from the low-frequency breakdown, where the contribution from the vector potential is extremely imbalanced with that from the scalar potential. As a result, the matrix representation of the EFIE operator is highly ill-conditioned and cannot be inverted reliably and efficiently.

Over the past few years, various approaches have been proposed to overcome the problem. As a quasi-Helmholtz decomposition and robust low-frequency solver, the loop-tree or loop-star decomposition [4–8] separates the surface current into solenoidal and irrotational parts to capture the inductance and capacitance physics, respectively. After frequency normalization, however, the matrix is still ill-conditioned giving rise to bad convergence especially for a dense mesh. Hence, robust preconditioning techniques, either based on the basis rearrangement [7] or incomplete factorization [9], are required to lower the condition number of the matrix. Unfortunately, these strategies indeed do not modify the spectrum properties of the EFIE kernel whose eigenvalues agglomerate around the origin and at infinity. Thanks to the self-regularizing feature of the EFIE, the Calderón multiplicative preconditioner [10–12] incorporating with the Buffa-Christiansen (BC) [13] or hierarchical basis functions [14] has been introduced to shift the spectrum of the preconditioned EFIE operator far away from both zero and infinity [15].

The recent developed augmented EFIE (A-EFIE) method [16–18], which employs current and charge as independent unknowns, can remedy the low-frequency breakdown and meanwhile avoid searching for loop bases. Furthermore, a similar A-EFIE method in conjugation with the Calderón multiplicative preconditioner [19] in nature removes the internal resonance corruption and preserves other merits of the EFIE.

One special method bridging electromagnetics and circuit theories is the partial electrical element circuit (PEEC) method [25–28]. Interestingly, it starts with the EFIE but does not has the low-frequency breakdown issue. This is due to the fact that it always considers the loss term in the system and employs the modified nodal analysis (MNA) to solve the resultant matrix equation [25, 26]. Hence, it obeys both Kirchhoff's voltage law (KVL) and Kirchhoff's current law (KCL) simultaneously in its solving process. This is equivalent to using the decoupled electric field and magnetic field for low frequencies [7]. PEEC has been conveniently applied in both time and frequency domains. And it has been successfully used for both coupling and scattering problems.

One reason that motivates us to use EFIE based method instead of the PEEC to solve low frequency problems is that we are looking

for a unified method that could solve both coupling and scattering problems based on the first principle supported by computational electromagnetic methods. PEEC is more popularly used for the coupling problem but not the scattering problem that is dominated by the wave physics. EFIE based methods were more popularly used for the scattering but not the coupling problem that is dominated by the circuit physics. Because the SPICE solver does not general accepts the retardation and does not favor densely coupled circuit network, most PEEC applications are static or quasi-static. EFIE based methods can use full wave dense matrixes and can be accelerated easily by many existing computational electromagnetics methods [20–24].

All algorithms mentioned above formulate the EFIE using the Lorentz-gauge Green's function [4, 16, 19]. In this paper, we investigate the Coulomb-gauge based EFIE and explore its application in solving the low-frequency problem, which is a new method that was not discussed before. It not only provides a novel low frequency EFIE method, but also a comparative study for EFIE based on two different gauges through physical interpretations and detailed numerical results. Relative to PEEC, the proposed method has less number of unknowns and provides a novel low-frequency solution for MOM based methods. With the help of the quasi-static approximation of the Coulomb gauge Green's function, the Coulomb-gauge EFIE is reformulated with a more elegant mathematical form and suitable to remedy the low-frequency breakdown of the EFIE operator. It will also be shown that most well-developed techniques adopted in the loop-tree or loop-star method can be directly applied to the Coulomb-gauge EFIE at low frequencies.

The paper is organized as follows. Section 2 describes the mathematical foundations and physical interpretations of the EFIE using the Coulomb-gauge Green's function. Particularly, the quasi-static version of the EFIE is reformulated and discretized by loop-tree basis functions with the frequency normalization and basis rearrangement strategies. Numerical examples are presented in Section 3 for demonstrating the validity of the Coulomb-gauge EFIE and comparing it to the Lorentz-gauge EFIE for the low-frequency problem. Section 4 summarizes the paper.

2. THEORY

2.1. Lorentz and Coulomb Gauges

The introduction of auxiliary potentials is a common procedure in dealing with electromagnetic problems. In this way one can recast Maxwell's equations into simple forms that can be numerically treated

by a variety of techniques. Due to a lack of uniqueness in the definition of potentials, we can conveniently impose conditions on potentials without affecting the results of electromagnetic fields. Such choices are gauges, and the most common ones are Lorentz and Coulomb gauges [29].

From Maxwell's equations, the scalar and vector potentials satisfy

$$\nabla^2\phi + j\omega(\nabla \cdot \mathbf{A}) = -\frac{\rho}{\epsilon} \tag{1}$$

$$\nabla^2\mathbf{A} + k^2\mathbf{A} - \nabla\left(\nabla \cdot \mathbf{A} + j\omega\mu\epsilon\phi\right) = -\mu\mathbf{J} \tag{2}$$

where ϵ and μ are the permittivity and permeability of homogeneous space, and $\mathbf{A}$ and ϕ are the vector and scalar potentials, respectively. Moreover, $k = \omega\sqrt{\mu\epsilon}$ is the wave number and ω is the angular frequency. In addition, harmonic time convention $e^{j\omega t}$ is assumed in this paper.

Using the Lorentz gauge $\nabla \cdot \mathbf{A}^L = -j\omega\mu\epsilon\phi^L$, we will decouple the pair of (1) and (2) and obtain the following two wave equations

$$\nabla^2\mathbf{A}^L + k^2\mathbf{A}^L = -\mu\mathbf{J} \tag{3}$$

$$\nabla^2\phi^L + k^2\phi^L = -\frac{\rho}{\epsilon} = \frac{1}{j\omega\epsilon}\nabla \cdot \mathbf{J} \tag{4}$$

The superscript "L" denotes the Lorentz gauge.

Alternative gauge for potentials is the Coulomb or transverse gauge, i.e., $\nabla \cdot \mathbf{A}^C = 0$. Consequently, the scalar potential satisfies the Poisson equation

$$\nabla^2\phi^C = -\frac{\rho}{\epsilon} = \frac{1}{j\omega\epsilon}\nabla \cdot \mathbf{J} \tag{5}$$

with the solution of

$$\phi^C = -\frac{1}{4\pi j\omega\epsilon}\int_{V'}\frac{\nabla' \cdot \mathbf{J}(\mathbf{r}')}{\mid \mathbf{r} - \mathbf{r}' \mid}d\mathbf{r}' \tag{6}$$

where the superscript "C" denotes the Coulomb gauge. The scalar potential is just the instantaneous Coulomb potential without the phase delay, which is the origin of the name "Coulomb gauge". The vector potential satisfies the wave equation

$$\nabla^2\mathbf{A}^C + k^2\mathbf{A}^C = -\mu\mathbf{J} + j\omega\mu\epsilon\nabla\phi^C \tag{7}$$

According to the Helmholtz' theorem, we can decompose the current density (or any vector field) into a solenoidal (transverse) part $\mathbf{J}^{sol}$ and an irrotational (lamellar or longitudinal) part $\mathbf{J}^{irr}$

$$\mathbf{J} = \mathbf{J}^{sol} + \mathbf{J}^{irr} \tag{8}$$

It has been shown that $\mathbf{J}^{sol}$ and $\mathbf{J}^{irr}$ could be constructed explicitly as follows [29]

$$\mathbf{J}^{irr} = -\frac{1}{4\pi}\nabla \int_{V'} \frac{\nabla' \cdot \mathbf{J}(\mathbf{r}')}{\mid \mathbf{r} - \mathbf{r}' \mid} d\mathbf{r}' \tag{9}$$

$$\mathbf{J}^{sol} = \frac{1}{4\pi}\nabla \times \int_{V'} \frac{\nabla' \times \mathbf{J}(\mathbf{r}')}{\mid \mathbf{r} - \mathbf{r}' \mid} d\mathbf{r}' \tag{10}$$

Taking the gradient of (6) together with (9) yields

$$\mathbf{J}^{irr} = j\omega\epsilon\nabla\phi^C \tag{11}$$

Substituting (11) into (7), we obtain

$$\nabla^2\mathbf{A}^C + k^2\mathbf{A}^C = -\mu\mathbf{J}^{sol} \tag{12}$$

Here the source of the wave equation for $\mathbf{A}^C$ can be expressed entirely in terms of the solenoidal (transverse) current, which is different from (3).

Critically different from the Lorentz gauge whose both potentials propagate with finite speed and retardation effects, the scalar potential under the Coulomb gauge is defined by the Poisson Equation (5). It means that the scalar potential "propagates" instantaneously everywhere in space. This is significantly different from the Lorentz gauge case. As to the vector potential, it is directly contributed from the solenoidal current $\mathbf{J}^{sol}$ through the Helmholtz Equation (12) instead of the total current $\mathbf{J}$. Based on (10), it is easily seen that $\mathbf{J}^{sol}$ is of the volume distribution. From the equivalent principle and extinction theorem, an inhomogeneous scattering problem involving a perfect electric conductor (PEC) can be converted into a radiation problem if we impress the induced current on the scatterer in the homogeneous space excluding the scatterer. In view of the Lorentz gauge, the equivalent surface current and charge can be regarded as surface sources for the wave equations of potentials as shown in (3) and (4). However, when the Coulomb gauge is adopted, the solenoidal current $\mathbf{J}^{sol}$ in (12) will extend over all space due to its nonlocal property from (10). Hence, regarding the Coulomb gauge, the nonphysical solenoidal $\mathbf{J}^{sol}$ cannot be numerically quantified by the surface integral equation (SIE) method.

2.2. Quasi-static Approximation of Coulomb Gauge Green's Function

Coulomb gauge Green's function enables us to resolve the nonphysical problem by replacing the solenoidal volume current $\mathbf{J}^{sol}$ with the

surface current $\mathbf{J}_s$. The Green's function equation pertaining to (12) is

$$\nabla^2 \bar{\mathbf{G}}_{\mathbf{A}}^{C} + k^2 \bar{\mathbf{G}}_{\mathbf{A}}^{C} = -\bar{\boldsymbol{\delta}}^{sol}(\mathbf{r} - \mathbf{r}') \tag{13}$$

Notice that the Coulomb gauge dyadic Green's function $\bar{\mathbf{G}}_{\mathbf{A}}^{C}$ is solenoidal because the solenoidal part of the Delta function is used as the excitation source. The solenoidal Delta function $\bar{\boldsymbol{\delta}}^{sol} = \frac{1}{4\pi}\nabla \times \nabla \times (\frac{\bar{\mathbf{I}}}{R})$ is an everywhere nonzero function of positions, albeit the Delta function $\bar{\boldsymbol{\delta}}(\mathbf{r} - \mathbf{r}') = -\frac{\bar{\mathbf{I}}}{4\pi}\nabla^2 \frac{1}{R}$ is nonzero only at $\mathbf{r} = \mathbf{r}'$. The Coulomb gauge Green's function is essentially the solenoidal component of the Lorentz gauge Green's function that can be found by [30]

$$\begin{aligned}
\bar{\mathbf{G}}_{\mathbf{A}}^{C} = \bar{\mathbf{G}}_{\mathbf{A}}^{L_{sol}}(\mathbf{r}, \mathbf{r}') &= \int_{V''} \bar{\boldsymbol{\delta}}^{sol}(\mathbf{r} - \mathbf{r}'') \cdot \bar{\mathbf{G}}_{\mathbf{A}}^{L}(\mathbf{r}'', \mathbf{r}') dV'' \\
&= \frac{1}{4\pi}\nabla \times \nabla \times \bar{\mathbf{I}} \int_{V''} \frac{\bar{\mathbf{G}}_{\mathbf{A}}^{L}(\mathbf{r}'', \mathbf{r}')}{\mid \mathbf{r} - \mathbf{r}'' \mid} dV'' \\
&= \bar{\mathbf{I}} g(\mathbf{r}, \mathbf{r}') + \frac{1}{k^2}\nabla\nabla \left(g(\mathbf{r}, \mathbf{r}') - g^s(\mathbf{r}, \mathbf{r}') \right)
\end{aligned} \tag{14}$$

where $g(\mathbf{r}, \mathbf{r}') = \frac{e^{-jkR}}{4\pi R}$ and $g^s(\mathbf{r}, \mathbf{r}') = \frac{1}{4\pi R}$ are the scalar Green's functions for the Helmholtz equation and Poisson equation, respectively.

Using the Coulomb gauge Green's function, the scattered electric field $\mathbf{E}^{sca}$ generated by the equivalent surface current $\mathbf{J}_s$ on the PEC is given as

$$\begin{aligned}
\mathbf{E}^{sca} = &-j\omega\mu \int_{S'} \bar{\mathbf{G}}_{\mathbf{A}}^{C}(\mathbf{r}, \mathbf{r}') \mathbf{J}_s(\mathbf{r}') d\mathbf{r}' \\
&+ \frac{1}{j\omega\epsilon}\nabla \int_{S'} g^s(\mathbf{r}, \mathbf{r}') \nabla' \cdot \mathbf{J}_s(\mathbf{r}') d\mathbf{r}'
\end{aligned} \tag{15}$$

Although the Coulomb gauge Green's function has more complex mathematical expression in comparison with the Lorentz gauge Green's function that is commonly employed in the mid-frequency electromagnetic problem, we will demonstrate that the quasi-static approximation of the Coulomb gauge Green's function shows a very elegant form and significant physical meaning for the low-frequency problem.

The Helmholtz' theorem can also be applied on a surface [31]. The surface current density $\mathbf{J}_s$ can be rigorously split into a solenoidal part and an irrotational part, i.e.,

$$\mathbf{J}_s = \mathbf{J}_s^{sol} + \mathbf{J}_s^{irr} \tag{16}$$

It is worth mentioning that the solenoidal surface current $\mathbf{J}_s^{sol}$ is fundamentally distinguished from the solenoidal volume current $\mathbf{J}^{sol}$. When the frequency is low, we have the quasi-static assumptions [1]

$$\mathbf{J}_s^{irr} \sim O(\omega), \quad \left|\mathbf{J}_s^{irr}\right| \ll \left|\mathbf{J}_s^{sol}\right|, \quad \omega \to 0 \tag{17}$$

Moreover, in the quasi-static regime, the operator $\nabla(g(\mathbf{r},\mathbf{r}') - g^s(\mathbf{r},\mathbf{r}'))$ in (14) can be approximated with the Taylor expansion. Ignoring the third-order term, we obtain

$$\begin{aligned}\nabla\left(g(\mathbf{r},\mathbf{r}') - g^s(\mathbf{r},\mathbf{r}')\right) &\approx \nabla\left(\frac{-jkR - (kR)^2/2}{4\pi R}\right) \\ &= -\frac{k^2}{8\pi}\nabla(R) = -\frac{k^2}{8\pi}\,\mathbf{e}_R\end{aligned} \tag{18}$$

where $\mathbf{e}_R = \mathbf{R}/R$ is the unit vector of $\mathbf{R}$. Substituting (16) and (18) into (15), the vector potential in (15) becomes

$$\mathbf{A}^C(\mathbf{r}) = \mu\int_{S'}\left(g(\mathbf{r},\mathbf{r}') - \frac{1}{8\pi}\nabla(\mathbf{e}_R)\right)\cdot\left(\mathbf{J}_s^{sol}(\mathbf{r}') + \mathbf{J}_s^{irr}(\mathbf{r}')\right)d\mathbf{r}' \tag{19}$$

With the help of integration by parts, (19) can be rewritten as

$$\begin{aligned}\mathbf{A}^C(\mathbf{r}) = \mu\int_{S'} g(\mathbf{r},\mathbf{r}')\mathbf{J}_s^{sol}(\mathbf{r}')d\mathbf{r}' + \mu\int_{S'} g(\mathbf{r},\mathbf{r}')\mathbf{J}_s^{irr}(\mathbf{r}')d\mathbf{r}' \\ -\mu\int_{S'}\frac{1}{8\pi}\mathbf{e}_R\nabla'\cdot\mathbf{J}_s^{irr}(\mathbf{r}')d\mathbf{r}'\end{aligned} \tag{20}$$

The irrotational $\mathbf{J}_s^{irr}$ and its divergence are on the order of the frequency ω, which are much smaller than the solenoidal $\mathbf{J}_s^{sol}$. As a result, the last two terms of (20) can be ignored under quasi-static assumptions. Finally, the vector-potential term can be approximated as

$$\mathbf{A}^C(\mathbf{r}) \approx \mu\int_{S'} g(\mathbf{r},\mathbf{r}')\mathbf{J}_s^{sol}(\mathbf{r}')d\mathbf{r}' \tag{21}$$

The EFIE represented by the Coulomb gauge Green's function at low frequencies is now modified to be a more elegant form

$$\begin{aligned}-\hat{\mathbf{n}}\times\mathbf{E}^{inc}(\mathbf{r}) = \hat{\mathbf{n}}\times\Bigg(-j\omega\mu\int_{S'} g(\mathbf{r},\mathbf{r}')\mathbf{J}_s^{sol}(\mathbf{r}')d\mathbf{r}' \\ +\frac{1}{j\omega\epsilon}\nabla\int_{S'} g^s(\mathbf{r},\mathbf{r}')\nabla'\cdot\mathbf{J}_s^{irr}(\mathbf{r}')d\mathbf{r}'\Bigg)\end{aligned} \tag{22}$$

where $\hat{\mathbf{n}}$ is the outward unit vector of the surface and $\mathbf{E}^{inc}$ denotes the incident electric field.

In the right-hand side of (22), the first term captures the inductive response corresponding to the magnetoquasistatic field produced by the solenoidal (eddy) current; and the second term captures the capacitive response corresponding to the electroquasistatic field produced by the irrotational current. At the low frequency, the irrotational term dominates over the solenoidal one leading to a null space of the above EFIE, which resembles the EFIE using the Lorentz gauge Green's function [1]. When the low-frequency breakdown problem inherent from the EFIE operator occurs, the matrix representation of the operator becomes extremely ill-conditioned.

2.3. Frequency Normalization and Basis Rearrangement

The remedy to rectify the low-frequency breakdown is to solve the problem in such a way that the inductive response and the capacitive response are well separated and accurately balanced. We use the quasi-Helmholtz decomposition adopted in the loop-tree and loop-star algorithms [4] to separate the total current, and normalize the produced matrix system to obtain a stable and balanced system with a good condition number.

First, we expand the surface current as follows

$$\mathbf{J}_s(\mathbf{r}') = \sum_{n=1}^{N_l} I_{Ln}\mathbf{J}_{Ln}(\mathbf{r}') + \sum_{n=1}^{N_t} I_{Tn}\mathbf{J}_{Tn}(\mathbf{r}') \tag{23}$$

where $\mathbf{J}_{Ln}(\mathbf{r}')$ is the loop basis function, $\mathbf{J}_{Tn}(\mathbf{r}')$ the tree basis function, and N_l and N_t are respectively the number of the loop and tree basis functions. The loop-tree basis functions can be spanned by a superposition of the RWG basis functions

$$\mathbf{J}_L(\mathbf{r}) = \bar{\mathbf{F}}_{LR} \cdot \mathbf{J}_{RWG}(\mathbf{r}) \tag{24}$$

$$\mathbf{J}_T(\mathbf{r}) = \bar{\mathbf{F}}_{TR} \cdot \mathbf{J}_{RWG}(\mathbf{r}) \tag{25}$$

where $\mathbf{J}_L(\mathbf{r})$ and $\mathbf{J}_T(\mathbf{r})$ are the column vectors including $\mathbf{J}_{Ln}(\mathbf{r})$ and $\mathbf{J}_{Tn}(\mathbf{r})$. Additionally, $\bar{\mathbf{F}}_{LR}$ and $\bar{\mathbf{F}}_{TR}$ are the connection matrices between the loop-tree and RWG basis functions [32].

Then, substituting (23) into (22) and applying the Galerkin testing procedure, we have the matrix equation

$$\begin{bmatrix} \bar{\mathbf{Z}}_{LL} & \bar{\mathbf{0}} \\ \bar{\mathbf{Z}}_{TL} & \bar{\mathbf{Z}}_{TT} \end{bmatrix} \cdot \begin{bmatrix} \mathbf{I}_L \\ \mathbf{I}_T \end{bmatrix} = \begin{bmatrix} \mathbf{V}_L \\ \mathbf{V}_T \end{bmatrix} \tag{26}$$

where

$$\bar{\mathbf{Z}}_{LL} = \bar{\mathbf{F}}_{LR} \cdot \bar{\mathbf{Z}}^V_{RWG} \cdot \bar{\mathbf{F}}^t_{LR} \tag{27}$$

$$\bar{\mathbf{Z}}_{LT} = \bar{\mathbf{F}}_{LR} \cdot \bar{\mathbf{Z}}^V_{RWG} \cdot \bar{\mathbf{F}}^t_{TR} \tag{28}$$

$$\bar{\mathbf{Z}}_{TT} = \bar{\mathbf{F}}_{TR} \cdot \bar{\mathbf{Z}}^S_{RWG} \cdot \bar{\mathbf{F}}^t_{TR} \tag{29}$$

and

$$\bar{\mathbf{Z}}^V_{RWG} = -j\omega\mu\langle \mathbf{J}_{RWG}(\mathbf{r}), g(\mathbf{r},\mathbf{r}'), \mathbf{J}^t_{RWG}(\mathbf{r}')\rangle \tag{30}$$

$$\bar{\mathbf{Z}}^S_{RWG} = -\frac{1}{j\omega\epsilon}\langle \nabla\cdot\mathbf{J}_{RWG}(\mathbf{r}), g^s(\mathbf{r},\mathbf{r}'), \nabla'\cdot\mathbf{J}^t_{RWG}(\mathbf{r}')\rangle \tag{31}$$

Here the superscript t denotes the transpose of the matrix. Likewise, the right-hand side of (26) can be represented by

$$\mathbf{V}_L = \bar{\mathbf{F}}_{LR}\cdot\bar{\mathbf{V}}_{RWG} \tag{32}$$

$$\mathbf{V}_T = \bar{\mathbf{F}}_{TR}\cdot\bar{\mathbf{V}}_{RWG} \tag{33}$$

where

$$\bar{\mathbf{V}}_{RWG} = -\langle \mathbf{J}_{RWG}(\mathbf{r}), \mathbf{E}^{inc}(\mathbf{r})\rangle \tag{34}$$

Finally, frequency normalization is implemented to produce a well-balanced matrix system

$$\begin{bmatrix} \omega^{-1}\bar{\mathbf{Z}}_{LL}\left(O\left(1\right)\right) & \bar{\mathbf{0}} \\ \bar{\mathbf{Z}}_{TL}\left(O\left(\omega\right)\right) & \omega\bar{\mathbf{Z}}_{TT}\left(O\left(1\right)\right) \end{bmatrix}\cdot\begin{bmatrix} \mathbf{I}_L\left(O\left(1\right)\right) \\ \omega^{-1}\mathbf{I}_T\left(O\left(1\right)\right) \end{bmatrix} = \begin{bmatrix} \omega^{-1}\mathbf{V}_L\left(O\left(1\right)\right) \\ \mathbf{V}_T\left(O\left(1\right)\right) \end{bmatrix} \tag{35}$$

The above can be expressed compactly as

$$\bar{\mathbf{Z}}'\cdot\mathbf{I}' = \mathbf{V}' \tag{36}$$

If we define

$$\bar{\mathbf{F}}'_{LR} = \frac{1}{\sqrt{-j\omega}}\bar{\mathbf{F}}_{LR} \tag{37}$$

$$\bar{\mathbf{F}}'_{TR} = \sqrt{-j\omega}\bar{\mathbf{F}}_{TR} \tag{38}$$

the frequency-scaled impedance matrix $\bar{\mathbf{Z}}'$ is

$$\bar{\mathbf{Z}}' = \begin{bmatrix} \bar{\mathbf{F}}'_{LR}\cdot\bar{\mathbf{Z}}^V_{RWG}\cdot\bar{\mathbf{F}}'^t_{LR} & \bar{\mathbf{0}} \\ \bar{\mathbf{F}}'_{TR}\cdot\bar{\mathbf{Z}}^V_{RWG}\cdot\bar{\mathbf{F}}'^t_{LR} & \bar{\mathbf{F}}'_{TR}\cdot\bar{\mathbf{Z}}^S_{RWG}\cdot\bar{\mathbf{F}}'^t_{TR} \end{bmatrix} \tag{39}$$

Obviously, the matrix representation by the Coulomb gauge Green's function is simpler and easier to be handled compared with that by the Lorentz gauge Green's function. However, for solving large-scale problems, the new matrix equation still converges very slowly when an iterative solver is used. Basis rearrangement [17] is utilized to further improve the convergence property of the matrix equation. It transforms the tree basis for irrotational current density to the pulse basis for charge density as it converges rapidly. When expanding the surface charge density on a connected object in terms of the pulse basis set, because of charge neutrality, the charge has only N_t degree

of freedom. A mapping matrix between charge pulse basis and tree expansion basis $\bar{\mathbf{K}}$ is thus defined as

$$-j\omega\mathbf{Q} = \bar{\mathbf{K}} \cdot \mathbf{I}_T \tag{40}$$

where $\mathbf{Q}$ is a column vector represents the charge density coefficients, and $\bar{\mathbf{K}} \in \mathbb{R}^{N_t \times N_t}$ is a sparse matrix given by

$$[\mathbf{K}]_{mn} = \langle P_m(\mathbf{r}), \nabla \cdot \mathbf{\Lambda}_n(\mathbf{r}) \rangle \tag{41}$$

where P_m represents the normalized pulse basis. The iterative solver is preferred for large scale computation. In this paper, the Krylov subspace iterative solver generalized minimal residual (GMRES) approach [33] is adopted with the restart number of 50. For acceleration purpose, the final matrix equation may be written in terms of a sequence of matrix-vector products as:

$$\begin{bmatrix} \bar{\mathbf{I}} & \bar{\mathbf{0}} \\ \bar{\mathbf{0}} & \left(\bar{\mathbf{K}}^t\right)^{-1} \end{bmatrix} \cdot \bar{\mathbf{Z}}' \cdot \begin{bmatrix} \bar{\mathbf{I}} & \bar{\mathbf{0}} \\ \bar{\mathbf{0}} & \bar{\mathbf{K}}^{-1} \end{bmatrix} \cdot \begin{bmatrix} \mathbf{I}_L \\ \mathbf{Q} \end{bmatrix} = \begin{bmatrix} w^{-1}\mathbf{V}_L \\ \left(\bar{\mathbf{K}}^t\right)^{-1} \cdot \mathbf{V}_T \end{bmatrix} \tag{42}$$

3. NUMERICAL RESULTS

This section presents three numerical examples to demonstrate properties of the Coulomb-gauge EFIE and compare it to the Lorentz-gauge EFIE for the low-frequency problem.

3.1. PEC Sphere

A canonical PEC sphere with the radius of 1 m is illuminated by an x-polarized plane wave propagating along the z direction. The sphere is discretized by triangular meshes involving 2427 inner edges. Figure 1 shows the E-plane bistatic radar cross section (RCS) at the frequency of 3×10^{-6} Hz calculated by the Coulomb-gauge and Lorentz-gauge EFIE approaches. The numerical techniques as described in Section 2.3, such as the loop-tree decomposition, frequency normalization, and basis rearrangement, are implemented for both approaches. The Coulomb-gauge and Lorentz-gauge EFIE approaches agree very well with the Mie series solution. Hence, the proposed method can solve the scattering problem at very low frequency.

Figure 2(a) shows the backward RCS as a function of the incident frequency. The numerical precision of the Coulomb-gauge EFIE approach is comparable to that of the Lorentz-gauge EFIE approach at low frequencies. However, it should be noted that both the Coulomb-gauge and Lorentz-gauge EFIE approaches using the loop-tree decompositions suffer from the high-frequency breakdown in contrast to the traditional EFIE method using the RWG basis

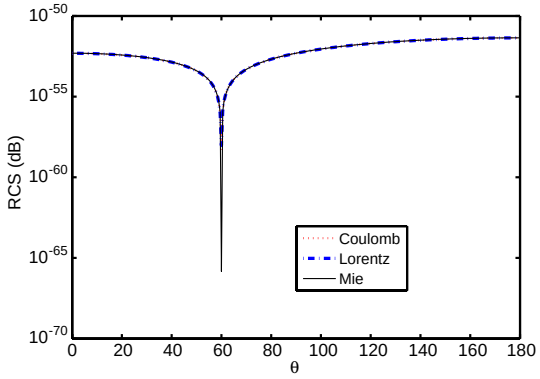

Figure 1. The E-plane bistatic RCS of a PEC sphere with the radius of 1 m at the frequency of 3×10^{-6} Hz. The incident plane wave is x-polarized and propagates along the z direction. The RCS is calculated by the Coulomb-gauge and Lorentz-gauge EFIE approaches.

functions. And this happens when the size of the object becomes comparable to the working wavelength.

Figure 2(b) illustrates the condition number of the impedance matrix for three EFIE schemes. In comparison with the RWG based EFIE method, the two loop-tree based EFIE approaches can improve the condition number of the impedance matrix significantly at low frequencies. The loop-tree based EFIE approaches push the eigenvalues away from the origin and thus alleviate the singularity or ill condition of the matrix.

Figure 2(c) presents the iteration numbers of the Lorentz-gauge and Coulomb-gauge EFIE approaches under the same tolerance of 5×10^{-6} condition. At low frequencies, both approaches achieve similar iteration numbers. When frequency keep increasing, the iteration number of both approaches increase, which again indicates the high-frequency breakdown problem of the loop-tree based EFIE scheme. Interestingly, quite different from the Coulomb-gauge EFIE, the iteration number of the Lorentz-gauge EFIE will significantly increase as the frequency increases, which can be seen in Figure 2(c). To understand the result, we compute the eigenvalue distributions of the two loop-tree based EFIE approaches at the frequency of 30 MHz as shown in Figure 3. The Coulomb-gauge EFIE applying the quasi-static approximation modifies the spectrum shape of the EFIE operator and compresses the eigenvalues in a more compact manner.

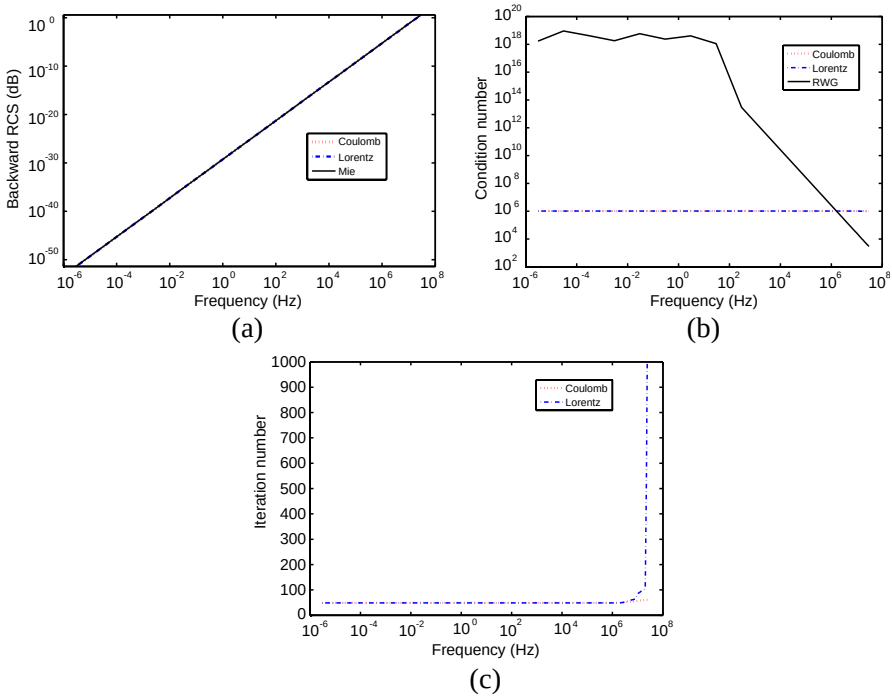

Figure 2. The simulation results for different EFIE schemes as a function of the incident frequency. (a) The backward RCS. (b) The condition number of the impedance matrix. (c) The number of iterations under the same tolerance condition.

3.2. Spiral Inductor

To benchmark that the new method can be used to solve the low frequency coupling type of problems, a spiral inductor is excited by a delta-gap source with the working frequency of 1 kHz. The inductor is backed by a ground plane with a size of 1.6 m × 2.0 m in the xoy plane. The distance between the inductor and the ground plane is 0.1 m. The width of the inductor is 0.15 m. The excitation is placed at one end of the inductor located at $z = 0.05$ m. The other end of the inductor is shorted to the ground. To evaluate the performances of the Lorentz-gauge and Coulomb-gauge EFIE approaches for the dense discretization breakdown problem, four different meshes, called A, B, C, and D, are generated ranging from coarse to dense patterns. The numbers of the RWG basis functions for the four meshes are 1028, 2298, 5430 and 9007, respectively.

Figure 4 plots the surface current distributions of the spiral

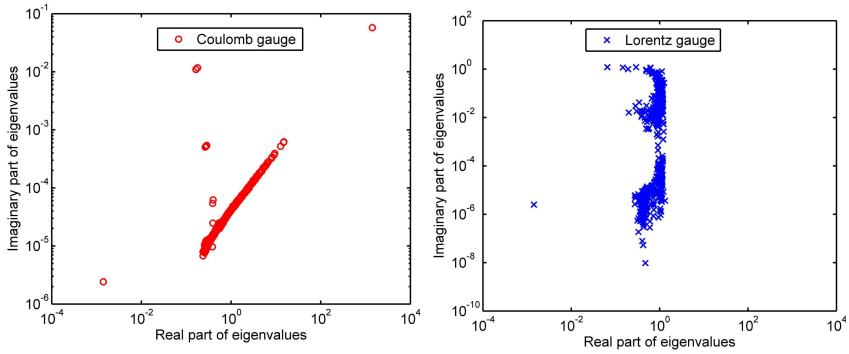

Figure 3. The eigenvalue distributions of the Coulomb-gauge and Lorentz-gauge EFIE approaches at the frequency of 30 MHz denoted by the arrows in Figure 2(c).

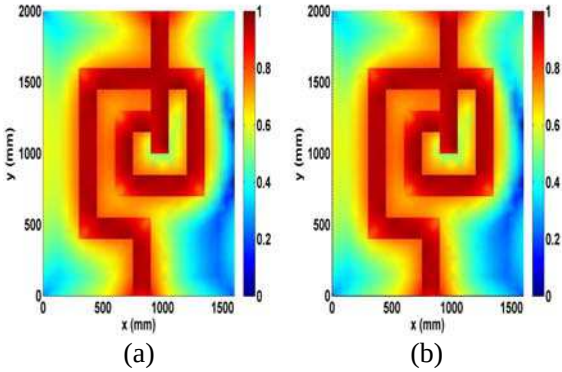

Figure 4. The surface current distributions of the spiral inductor with the dense mesh. (a) Lorentz-gauge EFIE. (b) Coulomb-gauge EFIE.

inductor with the dense mesh D. Obviously, both EFIE approaches with the loop-tree decompositions can capture the low-frequency circuit physics. The convergence behaviors of the GMRES solver using different mesh discretizations are demonstrated in Figure 5. The Coulomb-gauge EFIE approach converges slower as the mesh density increases because the spectrum properties of the EFIE operator cannot be changed by the frequency normalization and basis rearrangement strategies. So does the Lorenz-gauge EFIE approach. Table 1 lists the relevant computational information in detail. One can observe

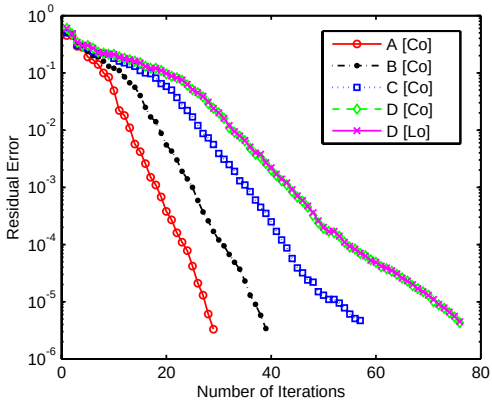

Figure 5. The convergence behaviors of the GMRES solver using different mesh discretizations where A, B, C, and D range from coarse to dense grids. The "Lo" and "Co" in the square brackets are the short notations of the Lorentz gauge and Coulomb gauge.

Table 1. The computational information of a spiral inductor working at 1 kHz. N_b and N_i are the number of the RWG basis functions and that of iterations, respectively. T_f and T_i are the CPU time respectively for the impedance matrix filling and each iteration step. L denotes the calculated inductance of the spiral inductor. The "Lo" and "Co" in the square brackets are the short notations of the Lorentz gauge and Coulomb gauge.

Mesh	A [Co]	B [Co]	C [Co]	D [Co]	D [Lo]
N_b	1028	2298	5403	9007	9007
N_i	29	39	57	76	76
T_f (S)	12	50	202	436	435
T_i (S)	0.034	0.051	0.192	0.526	0.526
L (10^{-2}H)	4.16	4.02	3.90	3.85	3.85

several common features for both EFIE approaches. On one hand, the inductance converges to a fixed value of 3.85×10^{-2} H when meshes become denser and denser. On the other hand, the computational costs of the Coulomb-gauge EFIE are almost the same as those of the Lorenz-gauge EFIE. Hence, the proposed method can be used to solve the low frequency coupling problem.

3.3. Interconnector

To validate the new coulomb-gauge EFIE approach for capturing the near field coupling that is important to IC and PCB technologies, an interconnector shown in Figure 6 is analyzed. There are two layers in the structure. Every finger on the top layer is connected with the bottom one through a via. The structure is excited by a delta-gap source located at the center of the top layer, as illustrated in Figure 6. The detail geometry dimensions can be obtained from [34]. The color map of Figure 6 also shows the calculated current distribution based on the Coulomb-gauge.

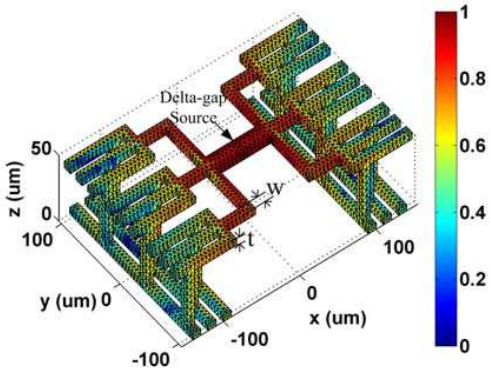

Figure 6. An interconnector structure with complicated geometries. The total size of the interconnector is 300 μm × 200 μm × 50 μm. The width and thickness of the strip are $w = 10\,\mu m$ and $t = 5\,\mu m$, respectively. A Delta-gap voltage source is imposed at the center of the top layer with a width of 20 μm. The structure is discretized with 8724 RWG bases. By using the Coulomb-gauge EFIE approach, the normalized current distribution of the interconnector at the frequency of 3 GHz is also shown.

The frequency dependent input reactance calculated respectively by the Lorentz-gauge and Coulomb-gauge EFIE approaches are listed in Table 2. The results obtained by the High Frequency Structure Simulator (HFSS) [35] software are also given as a reference. From the data it can be found that the input reactance is inversely proportional to frequency, which is exactly expected at the low frequency range. But when the frequency reaches 100 GHz (at which the size of the structure is around 1/10 of the wavelength), the inductive reactance will become significant. From this comparison, the Coulomb gauge based method works almost equally well as the Lorentz gauge based solution.

Table 2. An interconnector working at different frequencies is modeled by both Lorentz gauge and Coulomb gauge EFIE approaches. X denotes the calculated input reactance of the structure. N_i is the number of iterations. The "Lo" and "Co" in square brackets are short notations of the Lorentz gauge and Coulomb gauge.

Freq (GHz)	0.3	3	30	100
X (Ω) [Lo]	8.2×10^4	8.2×10^3	8.1×10^2	2.12×10^2
X (Ω) [Co]	8.2×10^4	8.2×10^3	8.2×10^2	2.45×10^2
X [HFSS]	8.32×10^4	8.86×10^3	8.76×10^2	2.29×10^2
N_i [Lo]	48	48	54	169
N_i [Co]	48	48	53	161

4. CONCLUSION

Using the Coulomb gauge, the electromagnetic fields can be expressed in terms of the scalar potential with the source of the irrotational current contributing only to the near-field and the vector potential with the source of the solenoidal volume current attributing to the transverse radiation fields. The Coulomb gauge Green's function conquers the difficulty in numerically quantifying the solenoidal volume current extending over all the space and connects the equivalent surface current with the scattered electrical field. Through the quasi-static approximation of the Coulomb gauge Green's function, the corresponding EFIE, which separates irrotational and solenoidal surface currents to capture circuit physics, can be applied to remedy the low-frequency breakdown problem. Naturally integrated with existing techniques, such as the loop-tree decomposition, frequency normalization, and basis rearrangement, the Coulomb-gauge EFIE achieves comparable accuracy and computational costs at low frequencies compared to the Lorentz-gauge EFIE. As the frequency increases, the Coulomb-gauge EFIE loses its accuracy but remains a good condition of the impedance matrix. Benchmarks are provided to demonstrate the discussed features of the Coulomb-gauge EFIE. This work provides a different angle and method of looking at low frequency problems of integral equations.

ACKNOWLEDGMENT

This work was supported in part by the Research Grants Council of Hong Kong (GRF 711511, 713011, and 712612), US AOARD FA2386-

12-1-4082, HKU Seed funding (201102160033), National Science Foundation of China (NSFC 61271158), and in part by the University Grants Council of Hong Kong (Contract No. AoE/P-04/08).

REFERENCES

1. Chew, W. C., M. S. Tong, and B. Hu, *Integral Equation Methods for Electromagnetic and Elastic Waves*, Morgan & Claypool, London, UK, 2009.
2. Araujo, M. G., J. M. Taboada, J. Rivero, and F. Obelleiro, "Comparison of surface integral equations for left-handed materials," *Progress In Electromagnetics Research*, Vol. 118, 425–440, 2011.
3. Rao, S. M., D. R. Wilton, and A. W. Glisson, "Electromagnetic scattering by surfaces of arbitrary shape," *IEEE Trans. Antennas Propag.*, Vol. 30, 409–418, 1982.
4. Wilton, D. R., J. S. Lin, and S. M. Rao, "A novel technique to calculate the electromagnetic scattering by surfaces of arbitrary shape," *URSI Radio Science Meeting Dig.*, Los Angeles, CA, 24–24, Jun. 1981.
5. Eibert, T. F., "Iterative-solver convergence for loop-star and loop-tree decompositions in method-of-moments solutions of the electric-field integral equation," *IEEE Antennas Propag. Mag.*, Vol. 46, 80–85, Jun. 2004.
6. Vecchi, G., "Loop-star decomposition of basis functions in the discretization of the EFIE," *IEEE Trans. Antennas Propag.*, Vol. 47, 339–346, Feb. 1999.
7. Zhao, J. S. and W. C. Chew, "Integral equation solution of Maxwell's equations from zero frequency to microwave frequencies," *IEEE Trans. Antennas Propag.*, Vol. 48, 1635–1645, Oct. 2000.
8. Yeom, J.-H., H. Chin, H.-T. Kim, and K.-T. Kim, "Block matrix preconditioner method for the electric field integral equation (EFIE) formulation based on loop-star basis functions," *Progress In Electromagnetics Research*, Vol. 134, 543–558, 2013.
9. Lee, J. F., R. Lee, and R. J. Burkholder, "Loop star basis functions and a robust preconditioner for EFIE scattering problems," *IEEE Trans. Antennas Propag.*, Vol. 51, 1855–1863, Aug. 2003.
10. Christiansen, S. H. and J. C. Nedelec, "A preconditioner for the electric field integral equation based on Calderón formulas," *SIAM J. Numer. Anal.*, Vol. 40, 1100–1135, Sep. 2002.

11. Yan, S., J. M. Jin, and Z. Nie, "EFIE analysis of low-frequency problems with loop-star decomposition and Calderón multiplicative preconditioner," *IEEE Trans. Antennas Propag.*, Vol. 58, 857–867, Mar. 2010.
12. Andriulli, F. P., K. Cools, H. Bagci, F. Olyslager, A. Buffa, S. Christiansen, and E. Michielssen, "A multiplicative Calderón preconditioner for the electric field integral equation," *IEEE Trans. Antennas Propag.*, Vol. 56, 2398–2412, Aug. 2008.
13. Buffa, A. and S. H. Christiansen, "A dual finite element complex on the barycentric refinement," *Math. Comput.*, Vol. 76, 1743–1769, 2007.
14. Valdes, F., F. P. Andriulli, K. Cools, and E. Michielssen, "High-order div- and quasi curl-conforming basis functions for Calderón multiplicative preconditioning of the EFIE," *IEEE Trans. Antennas Propag.*, Vol. 59, 1321–1337, Apr. 2011.
15. Andriulli, F. P., A. Tabacco, and G. Vecchi, "Solving the EFIE at low frequencies with a conditioning that grows only logarithmically with the number of unknowns," *IEEE Trans. Antennas Propag.*, Vol. 58, 1614–1624, May 2010.
16. Qian, Z. G. and W. C. Chew, "An augmented electric field integral equation for high-speed interconnect analysis," *Microw. Opt. Technol. Lett.*, Vol. 50, 2658–2662, Oct. 2008.
17. Qian, Z. G. and W. C. Chew, "Enhanced A-EFIE with perturbation method," *IEEE Trans. Antennas Propag.*, Vol. 58, 3256–3264, Oct. 2010.
18. Chen, Y. P., L. J. Jiang, Z. G. Qian, and W. C. Chew, "An augmented electric field integral equation for layered medium Green's function," *IEEE Trans. Antennas Propag.*, Vol. 59, 960–968, Mar. 2011.
19. Yan, S., J. M. Jin, and Z. P. Nie, "Analysis of electrically large problems using the augmented EFIE with a Calderón preconditioner," *IEEE Trans. Antennas Propag.*, Vol. 59, 2303–2314, Jun. 2011.
20. Pan, Y. C. and W. C. Chew, "A fast multipole method for embedded structure in a stratified medium," *Progress In Electromagnetics Research*, Vol. 44, 1–38, 2004.
21. Ergul, O. and L. Gurel, "Efficient solutions of metamaterial problems using a low-frequency multilevel fast multipole algorithm," *Progress In Electromagnetics Research*, Vol. 108, 81–99, 2010.
22. Bogaert, I., J. Peeters, and D. De Zutter, "Error control of the vectorial nondirective stable plane wave multilevel fast multipole

algorithm," *Progress In Electromagnetics Research*, Vol. 111, 271–290, 2011.

23. Pan, X.-M., L. Cai, and X.-Q. Sheng, "An efficient high order multilevel fast multipole algorithm for electromagnetic scattering analysis," *Progress In Electromagnetics Research*, Vol. 126, 85–100, 2012.
24. Wang, W. and N. Nishimura, "Calculation of shape derivatives with periodic fast multipole method with application to shape optimization of metamaterials," *Progress In Electromagnetic Research*, Vol. 127, 46–64, 2012.
25. Gope, D., A. Ruehli, and V. Jandhyala, "Solving low-frequency EM-CKT problems using the PEEC method," *IEEE Transactions on Advanced Packaging*, Vol. 30, No. 2, May 2007.
26. Jiang, L. J. and A. Ruehli, "On the frequency barrier of surface integral equations from a circuit point of view," *Progress In Electromagnetics Research Symposium Abstracts*, 46, Cambridge, USA, Jul. 5–8, 2010.
27. Song, Z., D. Su, F. Duval, and A. Louis, "Model order reduction for PEEC modeling based on moment matching," *Progress In Electromagnetics Research*, Vol. 114, 285–299, 2011.
28. Song, Z., F. Dai, D. Su, S. Xie, and F. Duval, "Reduced PEEC modeling of wire-ground structures using a selective mesh approach," *Progress In Electromagnetics Research*, Vol. 123, 355–370, 2012.
29. Jackson, J. D., *Classical Electrodynamics*, 3rd edition, Wiley India Pvt Ltd., 2007.
30. Nevels, R. D. and K. J. Crowell, "A Coulomb gauge analysis of a wire scatterer," *IEE Proc., Pt. H*, Vol. 137, 384–388, Dec. 1990.
31. Bladel, J., *Electromagnetic Field*, 3rd edition, Wiley-Interscience, 2007.
32. Chew, W. C., E. Michielssen, J. M. Song, and J. M. Jin, *Fast and Efficient Algorithms in Computational Electromagnetics*, Artech House, Inc., Norwood, MA, 2001.
33. Saad, Y. and M. H. Schultz, "GMRES: A generalized minimal residual algorithm for solving nonsymmetric linear systems," *SIAM J. Sci. Stat. Comput.*, Vol. 7, 856–869, Jul. 1986.
34. Chu, Y. H. and W. C. Chew, "Large-scale computation for electrically small structures using surface-integral equation method," *Microw. Opt. Technol. Lett.*, Vol. 47, No. 6, 525–530, Dec. 20, 2005.
35. http://www.ansys.com/Products/Simulation.